J. Fluid Mech. (1971), *vol.* 45, *part* 3, *pp.* 441–464
Printed in Great Britain

The source-sink flow in a rotating system and its oceanic analogy

By HAN-HSIUNG KUO
Woods Hole Oceanographic Institution, Woods Hole, Mass. 02543
AND GEORGE VERONIS
Department of Geology and Geophysics, Yale University, New Haven, Conn. 06520

(Received 3 March 1970)

Laboratory analogues of theoretical models of wind-driven ocean circulation are based on ideas presented by Stommel (1957). A particularly simple demonstration of the applicability of these ideas is contained in a paper by Stommel, Arons & Faller (1958). The present work develops the source-sink laboratory analogue of ocean circulation models to a point where chosen parametric values allow one to simulate the theoretical models of Stommel (1948) and Munk (1950) exactly. The investigation of the flow in a rotating cylinder generated by a source of fluid near the outer wall leads to a detailed description of the roles of the various boundary layers which occur. This knowledge is used to analyse the more complex source-sink flow in a pie-shaped basin. The laboratory analogue to the Stommel circulation model is analyzed in detail. It is shown that the change in the flow pattern brought about by a radial variation of the position of the eastern boundary in the pie-shaped basin is confined to the interior flow and the boundary layer is largely unaffected. When the bottom of the pie-shaped container slopes, the circulation pattern is changed significantly. For the particular case treated, the depth of the basin along the western boundary is unchanged and the maximum depth occurs at the southeast corner. The circulation generated by a source introduced at the apex of the pie has a gyre whose centre is shifted more toward the southwest corner than the corresponding centre of the gyre for a flat-bottomed basin. Two experiments are reported showing that the western boundary may separate because of the effect of bottom topography or because of the pressure of a cyclonic and an anti-cyclonic gyre generated by suitably placed sources and sinks.

1. Introduction

Consider a container of fluid which is rotating with a constant angular velocity about a vertical axis (z). The free surface of the fluid assumes a paraboloidal shape because of the balance of gravitational and centrifugal forces. Stommel (1957) pointed out that this variation in the depth of the fluid in a laboratory experiment serves to simulate the β-effect (the effect due to latitudinal variation of the Coriolis parameter) in the ocean.

It has long been recognized that the effect of a wind-stress at the surface of the

ocean is transmitted to the underlying fluid via an Ekman layer. When the wind-stress has a horizontal variation, the Ekman layer sucks fluid up from, or pumps fluid down into, the main body of the ocean. Hence, in a laboratory model the effect of a wind-stress can be simulated by a suitable source-sink flow.

Stommel, Arons & Faller (1958) took advantage of these analogies to set up an experimental demonstration of large scale ocean circulation in a laboratory model. Using geostrophic balance for the dynamics in the interior of the basin, they presented an elegant and simple analysis for the gross features of the circulation.

An investigation into the structure of the various boundary layers in the laboratory model reveals additional features which relate to the theoretical wind-driven circulation models of Stommel (1948) and Munk (1950). The present study is devoted to a discussion of these features, and to a re-examination of the flow in the light of recent developments of source-sink flow (Barcilon 1967; Hide 1967) and the general theory of rotating fluids (Greenspan 1968).

It is not our purpose to present a mathematical derivation of the different boundary layers that occur in rotating flows. However, it is necessary to make liberal use of the properties of these boundary layers. Therefore, the reader who wishes to verify the details must be familiar with the role of the Ekman boundary layer at the top and bottom of the basin and with the Stewartson boundary layers at the side walls. Greenspan's (1968) book contains a thorough treatment of these boundary layers.

In § 2 the equations for the source-sink flow are presented, and the essential features of the model are highlighted. The nature of the flow and the role and function of the different boundary layers are discussed in § 3, where all of the essential properties of the different boundary layers are used in order to analyse the flow in a cylindrical container with a single source at the wall. With E denoting the Ekman number (defined in § 2), it is shown that the $O(E^{\frac{1}{2}})$ upwelling velocity in the interior induces an $O(1)$ swirling flow, which is brought to zero at the side wall by a Stewartson layer of thickness $E^{\frac{1}{4}}$. Although the lowest order flow is thereby accounted for, a thorough understanding of the flow pattern is possible only by including an analysis of the $E^{\frac{1}{3}}$ layer at the side of the basin.

The detailed analysis of the flow in a cylinder brings out the essential manner in which the fluid progresses from its initial entry into the basin to its final swirling rise in the interior. The vertical redistribution of the entering fluid via the $E^{\frac{1}{3}}$ layer and the subsequent flow into the $E^{\frac{1}{4}}$ layer, and thence to the Ekman layer at the bottom, are necessary parts of the indirect circulation which leads to the upwelling of the free surface.

With the understanding gained from the detailed treatment in § 3, it is possible in § 4 to restrict the analysis of the flow in a pie-shaped basin to those features which are of most interest in the simulation of oceanic circulation. It is shown there that when the Froude number F is $O(1)$ the model of the laboratory situation is the mathematical analogue of Munk's (1950) wind-driven circulation model. The interior radial flow is determined by an equation which resembles the Sverdrup transport equation. Side-wall boundary layers are necessary to satisfy the dynamical boundary conditions. When $E^{\frac{1}{2}} \ll F \ll E^0$, the interior flow is satisfied by an equation which looks much like Stommel's (1948) equation for

wind-driven circulation, where the frictional force is assumed to be proportional to the velocity. The analysis that we present for this problem includes a sub-boundary layer to satisfy the non-slip condition at the wall, as well as a boundary layer at the radial (southern) wall.

We should mention here that calculations making use of variations of bottom topography for laboratory simulation of ocean circulation have been made by Pedlosky & Greenspan (1967) and by Beardsley (1969). However, we have made use of the paraboloidal shape of the free surface in order to simulate the β-effect for oceanic models, and we have reserved the variation of bottom topography to describe the analogous situation in nature. In this sense our simulation differs from that of the above authors. But our method of analysis does not differ substantially from theirs, and some of our results have been anticipated by Beardsley.

An investigation into the dynamical consequence of variations in the shape of the containing boundaries begins in § 4 with the study of the effect of a curved eastern boundary on the interior flow. The direction of the flow in the interior is completely determined by the shape of the eastern boundary. A simple analysis leads to the main features of the interior flow, and we show further that the intense western boundary flow is largely unaffected by the geometry of the eastern boundary.

That bottom topography can exercise a controlling influence on the flow pattern is well known. By introducing a small, uniform slope to the bottom boundary, we introduce a particularly simple example of the effects of bottom topography into the investigation. The interior flow pattern and the boundary layers are analyzed for the lowest-order solution. In this connexion it should be noted that the effects of topography manifest themselves principally via the change in the depth of the fluid so that in this way the role of bottom topography is similar to that of the paraboloidal free surface. However, the identification of the latter with the β-effect allows one to treat the two effects as separate ones and for physical purposes that is advantageous.

Section 5 contains experimental studies of the problems analysed in § 4 and a comparison between theory and experiment is presented. The agreement between the two is quite good with most discrepancies of the order of 10 % or less. The agreement in the boundary layers indicates that the more significant characteristics of the flow have been successfully analyzed. The interior flow patterns of the theory are all consistent with the experiments. In particular, the predicted differences determined among basins with uniform boundaries, with curved eastern boundaries and with varying topography, are all observed.

We conclude the study with two experimental models that contain features which can give rise to the separation of the western boundary current from the coast. A model with a sloping bottom confined to a corner of the basin shows that separation as predicted by Warren (1963) and Holland (1967) actually occurs experimentally. In the second model a source and a sink are introduced at interior locations. They are meant to simulate wind-stress gyres which are respectively cyclonic and anti-cyclonic. The results show that the two converging western boundary currents leave the coast when they meet and are directed into the interior.

2. Mathematical formulation

2.1. *Basic equations*

Consider a container of fluid rotating about the vertical (z) axis with uniform angular velocity Ω (figure 1). The steady, linearized, non-dimensional equations of motion for a viscous incompressible fluid written in terms of the rotating frame of reference are

$$2\mathbf{k}\times\mathbf{v} = -\nabla p + E\nabla^2\mathbf{v}, \tag{2.1}$$

$$\nabla.\mathbf{v} = 0, \tag{2.2}$$

where $E = \nu/\Omega a^2$ is the Ekman number and ν is the kinematic viscosity. Lengths are scaled in terms of the radius a of the container. The pressure is scaled by $\rho\Omega a u^*$ where ρ is the density and u^* is a characteristic velocity which will be related to the upwelling of the free surface when a source is introduced.

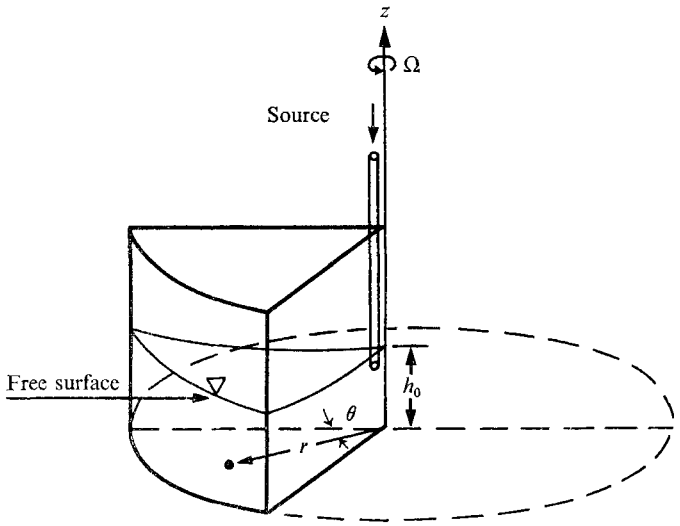

FIGURE 1. The general configuration of the source-sink flow in a rotating container.

The height of the paraboloidal free surface associated with pure, rigid-body rotation is written in terms of cylindrical co-ordinates (r, θ, z) as

$$h(r) = h_0\left(1+\frac{\Omega^2 a}{2gh_0}r^2\right), \tag{2.3}$$

where h_0 is the height of the fluid at the axis of rotation and g is gravitational aeeeleration. The equation for the free surface is

$$z = h(r) + \zeta(r, \theta, t), \tag{2.4}$$

where $\zeta(r, \theta, t)$ is the change of height of the surface due to the influx from the source. If particles initially on the free surface remain there, the linearized free surface condition is given by

$$w = \frac{\partial\zeta}{\partial t} + u\frac{\partial h}{\partial r}. \tag{2.5}$$

The linearized boundary condition for the flow in the container when a constant source flow is introduced are as follows:

(i) At $z = h$,

$$w = Fru + \dot{\zeta}, \tag{2.6}$$

where $F = \Omega^2 a/g$ is the Froude number and is considered in the range $E^0 \geqslant F \geqslant E^{\frac{1}{2}}$ and $\dot{\zeta} = \partial\zeta/\partial t$ is constant. For a linear problem it is necessary that $\dot{\zeta} = O(E^{\frac{1}{2}})$.

(ii) At the bottom ($z = 0$) of the container,

$$\mathbf{v} = 0. \tag{2.7}$$

(iii) At the side walls of the container,

$$\mathbf{v} = 0. \tag{2.8}$$

(iv) A transport condition associated with the influx from the source will be specified later.

2.2. *Interior flow*

Let the solution of equations (2.1) and (2.2) under the boundary conditions (i), (ii), (iii) and (iv) consist of an interior part (indicated by subscript I) which holds throughout the entire region, and a boundary-layer part (with subscript b for bottom boundary layer and s for side-wall layer), which add to the interior solution to meet the required boundary conditions and which decay with distance from the boundary. The solutions are obtained by standard asymptotic expansion in terms of the Ekman number. The results for the interior flow can be summarized as follows:

(i) To $O(E)$ the interior flow obeys the geostrophic and hydrostatic relations,

$$2\mathbf{k} \times \mathbf{v}_I = -\nabla p_I. \tag{2.9}$$

(ii) The interior vertical velocity w_I is $O(E^{\frac{1}{2}})$ and is independent of z.

(iii) The boundary condition at the free surface for the interior flow is derived from (2.6) as,

$$\text{at} \quad z = h, \quad w_I(r, \theta, h) = Fru_I + \dot{\zeta}, \tag{2.10}$$

where $\dot{\zeta}$ is $O(E^{\frac{1}{2}})$. The condition at the bottom is obtained from the well-known Ekman boundary-layer theory and can be written as,

$$\text{at} \quad z = 0, \quad w_I(r, \theta, 0) = \frac{E^{\frac{1}{2}}}{2}\left[\frac{1}{r}\frac{\partial}{\partial r}(rv_I) - \frac{1}{r}\frac{\partial}{\partial \theta}u_I\right]. \tag{2.11}$$

Since by statement (i) w_I is independent of z, the following relation holds:

$$w_I(r, \theta, h) = w_I(r, \theta, 0). \tag{2.12}$$

Accordingly, by statement (iii),

$$\tfrac{1}{2}E^{\frac{1}{2}}\left[r\frac{\partial}{\partial r}(rv_I) - \frac{1}{r}\frac{\partial}{\partial \theta}u_I\right] = Fru_I + \dot{\zeta}. \tag{2.13}$$

In terms of pressure, (2.13) can be written as

$$\frac{E^{\frac{1}{2}}}{2F}\left[\frac{1}{r}\frac{\partial}{\partial r}\left(r\frac{\partial}{\partial r}p_I\right) + \frac{1}{r^2}\frac{\partial^2 p_I}{\partial \theta^2}\right] + \frac{\partial p_I}{\partial \theta} = \frac{2\dot{\zeta}}{F}. \tag{2.14}$$

Since the vertical velocity is $O(E^{\frac{1}{2}})$, the above equation holds when F is $O(E^{\frac{1}{2}})$. In this case, u_I is $O(E^0)$. When F is $O(E^0)$, u_I should be $O(E^{\frac{1}{2}})$ as indicated by (2.10) and, if $v_I \leqslant O(E^{\frac{1}{2}})$, the value of w_I at $z = 0$ is $O(E)$. Therefore, it follows from (2.10), that

$$Fru_I + \dot{\zeta} = 0,$$

or

$$\partial p_I/\partial\theta = 2\dot{\zeta}/F. \tag{2.15}$$

When the interior flow is axisymmetric, both u_I and $\partial p_I/\partial\theta$ will vanish. The governing equation of the interior flow is then

$$\tfrac{1}{2}E^{\frac{1}{2}}r\frac{\partial}{\partial r}(rv_I) = \dot{\zeta},$$

or

$$\frac{1}{r}\frac{\partial}{\partial r}\left(r\frac{\partial p_I}{\partial r}\right) = 4\dot{\zeta}/E^{\frac{1}{2}}. \tag{2.16}$$

This equation is applicable to certain flows in a right cylindrical container.

If $E^{\frac{1}{2}} \ll 2F \ll 1$, equation (2.14) can be used for the interior flow. Enough arbitrariness is present to satisfy the condition that the normal velocity vanish at the boundaries. However, the non-slip condition cannot be satisfied. Equation (2.14) and the pertinent boundary conditions combine to make this problem the exact laboratory analogue of Stommel's (1948) model of the wind-driven ocean circulation. When F is $O(E^0)$, equation (2.15) describes the flow in the interior of the basin. This equation is analogous to the Sverdrup (1947) transport equation on the β-plane. When side-wall viscous layers are added, the resulting problem takes the exact form of Munk's (1950) model for the wind-driven ocean circulation.

Before going on to discuss these source-sink analogues to ocean circulation, we shall examine the flow in a cylindrical container in detail, so as to understand the physical nature of the side-wall viscous layers.

3. The source-sink flow in a cylindrical container

3.1. *Interior flow*

Let a source be introduced at $r = 1$ and $\theta = 0$ at the side wall of a cylindrical container. The interior flow is axially symmetric to $O(E^{\frac{1}{2}})$, and is governed by (2.16). The solution obtained under the conditions that the velocity be finite at the centre, and that there be no influx at the side wall, is

$$p_I = \dot{\zeta}/E^{\frac{1}{2}}(r^2 - 1). \tag{3.1}$$

The corresponding velocities are

$$v_I = \dot{\zeta}r/E^{\frac{1}{2}}, \quad u_I = 0. \tag{3.2}$$

The interior solution gives an $O(E^0)$ zonal velocity, which does not vanish at the side wall. Viscous boundary layers are required, so that the non-slip condition can be satisfied at the wall. The $O(E^0)$ interior pressure is independent of θ, and the $O(E^0)$ radial velocity vanishes. However, the non-uniformity of the source in the θ direction will introduce an $O(E^{\frac{1}{2}})$ radial flow. Hence, a more general form for the interior pressure should be written as

$$p_I = \dot{\zeta}/E^{\frac{1}{2}}(r^2 - 1) + E^{\frac{1}{2}}p_1(r, \theta), \tag{3.3}$$

where the last term represents the $O(E^{\frac{1}{2}})$ correction to the interior flow and $p_1(\theta)$ is $O(1)$. The detailed discussion of the nature of the viscous boundary layers and the $O(E^{\frac{1}{2}})$ correction to the interior flow are given below.

3.2. *Side-wall viscous boundary*

Viscous boundary layers must be added to the interior solution in order to meet the conditions at the side wall. A detailed discussion of these boundary layers in rotating fluids is contained in Greenspan (1968). Here, we simply outline properties of the boundary layers which are pertinent to the flow being considered.

The azimuthal velocity (3.2) does not satisfy the non-slip boundary condition at the wall. The latter condition is met by adding a viscous boundary layer of thickness $E^{\frac{1}{4}}$. The magnitude of the variables in the $E^{\frac{1}{4}}$ layer are

$$P_s \sim O(E^{\frac{1}{4}}),\ u_s \sim O(E^{\frac{1}{2}}),\ v_s \sim O(E^0) \text{ and } w_s \sim O(E^{\frac{1}{4}}).$$

In the interior, the azimuthal flow is independent of the vertical co-ordinate. The non-uniformity of the source in the z-direction is taken care of by a viscous boundary layer of thickness $E^{\frac{1}{3}}$, whose variables have the following magnitudes: $P_s \sim O(E^{\frac{1}{2}})$, $u_s \sim O(E^{\frac{1}{2}})$, $v_s \sim O(E^{\frac{1}{6}})$ and $w_s \sim O(E^{\frac{1}{6}})$. The $E^{\frac{1}{3}}$ layer also serves to bring the lowest-order vertical velocity to zero at the side wall. If the source is non-uniform in the θ direction, an $O(E^{\frac{1}{2}})$ radial flow will be induced in the interior, and the $O(E^{\frac{1}{2}})$ radial velocity from a side-wall boundary layer will combine with it to satisfy the boundary condition of vanishing radial velocity at the wall.

Following Greenspan (1968), we shall treat the $E^{\frac{1}{3}}$ and $E^{\frac{1}{4}}$ layers simultaneously *via* the following equations for the side-wall layers:

$$\left.\begin{aligned} 2v_s &= \frac{\partial p_s}{\partial \eta}, \\ 2u_s = -\frac{\partial p_s}{\partial \theta} + E\frac{\partial^2 v_s}{\partial \eta^2} &= -\frac{\partial p_s}{\partial \theta} + \frac{E}{2}\frac{\partial^3 p_s}{\partial \eta^3}, \\ 0 &= -\frac{\partial p_s}{\partial z} + E\frac{\partial^2 w_s}{\partial \eta^2}, \\ \frac{\partial u_s}{\partial \eta} + \frac{\partial v_s}{\partial \theta} + \frac{\partial w_s}{\partial z} &= 0, \end{aligned}\right\} \tag{3.4}$$

where $\eta = r - 1$. At the top and bottom of the side-wall layers, the flow is determined by Ekman boundary layers. A source given by $T(1, \theta, z)$ is assumed to inject fluid into the container through the side wall.

The boundary condition for the above equations can be obtained as

$$\left.\begin{aligned} &\text{(i)} \quad \text{at } z = h, && w_s = 0 + O(E^{\frac{1}{2}}); \\ &\text{(ii)} \quad \text{at } z = 0, && w_s = \tfrac{1}{4}E^{\frac{1}{2}}(\partial^2 p_s/\partial \eta^2); \\ &\text{(iii)} \quad \text{at } \eta = 0, && v_s = -v_I(1, \theta) = -\zeta/E^{\frac{1}{2}} + O(E^{\frac{1}{2}}); \\ & && w_s = 0; \\ &\text{(iv)} \quad \text{at } \eta = 0, && u = -\tfrac{1}{2}E^{\frac{1}{2}}(\partial p_1/\partial \theta) + u_s = -T_1(1, \theta, z). \end{aligned}\right\} \tag{3.5}$$

Here, we have made use of the Ekman layer near $z = 0$ to derive equation (ii). Relations (iii) and (iv) describe the condition that the total velocity vanishes at

the wall except at the inflow point. The relation between the total transport Q, and the source, $T(1,\theta,z)$, is

$$Q = \int_0^h \int_0^{2\pi} T(1,\theta,z)\, d\theta\, dz, \tag{3.6}$$

and Q is of $O(E^{\frac{1}{2}})$. If a concentrated line source is located at the point $r = 1$ and $\theta = 0$, the source function $T(1,\theta,z)$ can be regarded as a delta function at the point.

The solution of (3.4), together with the boundary conditions (i), (ii), (iii), is easily derived from the general solution to (3.4) given by Greenspan (1968, p. 112), who made use of the method introduced by Stewartson (1957):

$$\begin{aligned} p_s = {} & 2(Eh^2)^{\frac{1}{4}} \frac{\dot{\zeta}}{E^{\frac{1}{2}}} \exp\left[-(Eh^2)^{-\frac{1}{4}}(1-r)\right] \\ & - 2\sum_{n=1}^{\infty} \left\{ \frac{1}{2n\pi} \frac{\dot{\zeta}}{(Eh^2)^{\frac{1}{4}}} \left[\frac{1}{\gamma_{n1}} \exp\left[-\gamma_{n1}(1-r)\right] - \frac{1}{\gamma_{n3}} \exp\left[-\gamma_{n3}(1-r)\right] \right] \right. \\ & - \left(\frac{1}{\gamma_{n2}} - \frac{1}{\gamma_{n3}} \right)^{-1} \left[\left(\frac{1}{\gamma_{n1}} - \frac{1}{\gamma_{n3}} \right) \frac{1}{2n\pi} \frac{\dot{\zeta}}{(Eh^2)^{\frac{1}{4}}} + \frac{h}{n\pi} T_n^0 \right. \\ & \left. + \sum_{k=1}^{\infty} \left(\frac{(n\pi/h)\, T_{n,s}^k - kT_{n,c}^k}{k^2 + (n^2\pi^2/h^2)} \sin k\theta + \frac{(n\pi/h)\, T_{n,c}^k + kT_{n,s}^k}{k^2 + (n^2\pi^2/h^2)} \cos k\theta \right) \right] \\ & \left. \times \left(\frac{1}{\gamma_{n2}} \exp\left[-\gamma_{n2}(1-r)\right] + \frac{1}{\gamma_{n3}} \exp\left[-\gamma_{n3}(1-r)\right] \right) \right\} \cos \frac{n\pi z}{h}, \end{aligned} \tag{3.7}$$

where

$$\gamma_{n1} = \left(\frac{2n\pi}{Eh}\right)^{\frac{1}{3}}, \quad \gamma_{n2} = \left(\frac{2n\pi}{Eh}\right)^{\frac{1}{3}} \exp\left(\tfrac{1}{3}i\pi\right), \quad \gamma_{n3} = \left(\frac{2n\pi}{Eh}\right)^{\frac{1}{3}} \exp\left(-\tfrac{1}{3}i\pi\right),$$

$$T_{n,s}^k = \frac{1}{\pi} \int_0^{2\pi} \frac{2}{h} \int_0^h T(1,\theta,z) \cos \frac{n\pi z}{h} \sin k\theta\, dz\, d\theta,$$

$$T_{n,c}^k = \frac{1}{\pi} \int_0^{2\pi} \frac{2}{h} \int_0^h T(1,\theta,z) \cos \frac{n\pi z}{h} \cos k\theta\, dz\, d\theta,$$

$$T_n^0 = \frac{1}{2\pi} \int_0^{2\pi} \frac{2}{h} \int_0^h T(1,\theta,z) \cos \frac{n\pi z}{h}\, dz\, d\theta.$$

The terms with exponential factor $(Eh^2)^{-\frac{1}{4}}$ describe the behaviour in the $E^{\frac{1}{4}}$ layer, and those with γ_n give the form for the pressure in the $E^{\frac{1}{3}}$ layer. The $E^{\frac{1}{4}}$ layer brings the zonal velocity to zero at the side wall, and the $E^{\frac{1}{3}}$ layer adjusts the non-uniformity of the source in the z-direction and brings the lowest-order vertical velocity to zero at the side.

The requirement set by boundary condition (iv) on u_s, together with the solution of p_s, gives the following relation for p_1:

$$\text{at} \quad r = 1, \quad -\frac{E^{\frac{1}{2}}}{2} \frac{\partial p_1}{\partial \theta} = -\hat{T}(1,\theta) + \dot{\zeta}/2h, \tag{3.8}$$

where

$$\hat{T}(1,\theta) = \frac{1}{h} \int_0^h T(1,\theta,z)\, dz. \tag{3.9}$$

Since $\dot{\zeta} = Q/\pi$ the term $\dot{\zeta}/2h = Q/2\pi h$ represents the $O(E^{\frac{1}{2}})$ uniform radial velocity of the $E^{\frac{1}{4}}$ layer at the wall. The equation indicates that the non-uniformity of the source in the θ-direction is adjusted by the $O(E^{\frac{1}{2}})$ interior flow.

3.3. *The $O(E^{\frac{1}{2}})$ correction to the interior flow*

The analysis in the previous section shows that a non-axisymmetric $O(E^{\frac{1}{2}})$ interior horizontal flow is necessary to adjust the non-uniformity of the source in the θ-direction. The equations for the $O(E^{\frac{1}{2}})$ correction to the interior flow can be derived from the results obtained in § (2.1), because the interior is geostrophic to $O(E)$. In this case, p_1 is determined by

$$\epsilon\left[\frac{1}{r}\frac{\partial}{\partial r}\left(r\frac{\partial p_1}{\partial r}\right)+\frac{1}{r^2}\frac{\partial^2 p_1}{\partial\theta^2}\right]+\frac{\partial p_1}{\partial\theta}=0, \tag{3.10}$$

where $\epsilon = E^{\frac{1}{2}}/2F$. For simplicity, we shall treat the case $\epsilon \ll 1$, since all of the required information can be obtained more simply.

The solution of (3.10), together with the boundary condition (3.8), is obtained by asymptotic expansion. The 'interior' solution of (3.10) is obtained by dropping the term with ϵ, so that

$$\partial p_1/\partial\theta = 0,$$

which has the solution $p_1 = f(r)$, and represents an $O(E^{\frac{1}{2}})$ correction to the zonal velocity. But the $O(E^0)$ zonal velocity has already been determined, and our present interest is in completing the solution to include the largest contribution to the radial velocity. It is the latter which is necessary to adjust the non-axisymmetric source flow to the interior region. Hence, we discard $f(r)$.

To determine the $O(E^{\frac{1}{2}})$ radial velocity, we stretch the radial co-ordinate near $r = 1$ by

$$\partial/\partial r = \epsilon^{-\frac{1}{2}}\partial/\partial\xi, \quad r-1 = \epsilon^{\frac{1}{2}}\xi, \tag{3.11}$$

and (3.10) reduces to

$$\frac{\partial^2 p_1}{\partial\xi^2}+\frac{\partial p_1}{\partial\theta} = 0+O(E^{\frac{1}{2}}). \tag{3.12}$$

This equation is solved by Fourier series. The final result reads

$$p_1 = \sum_{n=1}^{\infty}\exp\left[-\sqrt{\frac{n}{2\epsilon}}(1-r)\right]\left\{\left[M_n\cos\sqrt{\frac{n}{2\epsilon}}(1-r)-N_n\sin\sqrt{\frac{n}{2\epsilon}}(1-r)\right]\sin n\theta\right.$$
$$\left.+\left[N_n\cos\sqrt{\frac{n}{2\epsilon}}(1-r)+M_n\sin\sqrt{\frac{n}{2\epsilon}}(1-r)\right]\cos n\theta\right\}, \tag{3.13}$$

where

$$M_n = \frac{1}{n\pi}\int_0^{2\pi}\frac{2}{E^{\frac{1}{2}}}\hat{T}(1,\theta)\sin n\theta\,d\theta,$$

$$N_n = \frac{1}{n\pi}\int_0^{2\pi}\frac{2}{E^{\frac{1}{2}}}\hat{T}(1,\theta)\cos n\theta\,d\theta.$$

This $O(E^{\frac{1}{2}})$ interior horizontal flow is induced by the non-uniformity of the source in the θ-direction, and balances the radial flow of the $E^{\frac{1}{4}}$ layer at the side wall. The non-uniformity of the source is therefore smoothed out by the $O(E^{\frac{1}{2}})$ interior horizontal flow in a frictional layer of thickness $\epsilon^{\frac{1}{2}}$ at the side wall. When ϵ is $O(1)$, the solution corresponding to (3.13) is expressed in terms of Bessel functions, and the flow exists throughout the interior.

A schematic picture of the source-sink flow is exhibited in figure 2. The transport of $O(E^{\frac{1}{2}})$ enters the tank and is distributed vertically in the $E^{\frac{1}{3}}$ layer, which smooths out the non-uniformity in the z-direction. The fluid flows into the $E^{\frac{1}{4}}$ layer, and then to the bottom Ekman layer, from which it flows upward into the interior as the free surface rises. The $O(E^{\frac{1}{2}})$ upwelling velocity of the interior induces a swirl velocity of $O(1)$. The swirl velocity is brought to zero at the side wall by the $E^{\frac{1}{4}}$ layer. The vertical velocity of the lowest-order ($E^{\frac{1}{6}}$) is adjusted to zero at the side wall by the $E^{\frac{1}{3}}$ layer. The non-uniformity of the source in the θ-direction causes an $O(E^{\frac{1}{2}})$ interior horizontal flow.

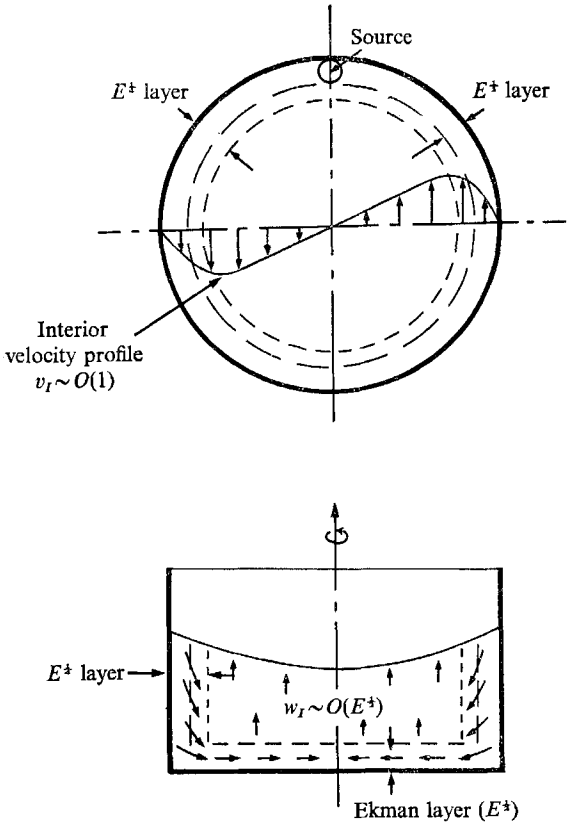

FIGURE 2. The general results of the source-sink flow in a rotating cylindrical container.

4. The source-sink flow in a pie-shaped basin

4.1. *The interior and boundary-layer flows*

In § 2 we established the fact that the equations which determine the flow in a pie-shaped basin depend on the Froude number F. When $F = O(E^0)$ the flow is determined by the laboratory analogue (2.15) of the Sverdrup transport equation and, when viscous side-wall layers are added, the boundary-value problem takes the form of Munk's model of wind-driven ocean circulation. When $E^0 \gg F \gg E^{\frac{1}{2}}$, the effects of bottom friction are confined to a region of $O(E^{\frac{1}{2}}/2F)$ near the outer

wall. To satisfy all the boundary conditions at the side wall, it is necessary to add an $E^{\frac{1}{4}}$ Stewartson layer, whose thickness was found (from § 3) to be $(Eh^2)^{\frac{1}{4}}$. Hence, from the ratio of these two thicknesses, the Stewartson layer can be regarded as a sub-boundary layer if $E^{\frac{1}{4}}/2Fh^{\frac{1}{2}} \gg 1$. In this case, the lowest-order problem for the interior flow is the exact laboratory analogue to Stommel's model of the wind-driven circulation of the ocean. That is the problem on which we shall focus our attention here.

The equation for the interior flow given by

$$\epsilon\left[\frac{1}{r}\frac{\partial}{\partial r}\left(r\frac{\partial p_I}{\partial r}\right)+\frac{1}{r^2}\frac{\partial^2 p_I}{\partial\theta^2}\right]+\frac{\partial p_I}{\partial\theta}=2\dot{\zeta}/F, \tag{4.1}$$

$$\epsilon = E^{\frac{1}{2}}/2F \ll 1, \tag{4.2}$$

together with the boundary condition $p_I = 0$ along the side wall, will be solved by the method of singular perturbation (Cole 1968). If p_I and its derivatives are of the same order, (4.1) can be written to $O(\epsilon)$ as

$$\partial p_I/\partial\theta = 2\dot{\zeta}/F. \tag{4.3}$$

The solution is

$$p_I = \frac{2\dot{\zeta}}{F}\theta + f(r). \tag{4.4}$$

There is obviously not enough arbitrariness to satisfy the boundary conditions. Hence, the condition that p_I and its derivatives be $O(E^0)$ must be relaxed. Proceeding in the usual manner, we stretch the co-ordinate near $\theta = 0$ as

$$\frac{\partial}{\partial\theta} = \epsilon^{-1}\frac{\partial}{\partial\xi}, \quad \theta = \epsilon\xi, \tag{4.5}$$

and can reduce (4.1) to

$$\frac{1}{r^2}\frac{\partial^2\overline{p}_I}{\partial\xi^2}+\frac{\partial\overline{p}_I}{\partial\xi} = 0+O(\epsilon), \tag{4.6}$$

with the solution

$$\overline{p}_I = A(r)\,e^{-\xi r^2}+B(r), \tag{4.7}$$

where the overbar corresponds to the Stommel boundary-layer contribution. The sum of the solutions (4.4) and (4.7) can satisfy the boundary condition at $\theta = 0$ and $\theta = \theta_0$ to order ϵ. The appropriate solution is

$$p_I = \frac{2\dot{\zeta}}{F}[(\theta-\theta_0)+\theta_0\exp(-r^2\theta/\epsilon)]. \tag{4.8}$$

The boundary layer described by the exponential term corresponds to Stommel's side boundary layer. It is due to the concentrated effect of bottom friction near the western ($\theta = 0$) boundary. We shall refer to it as the Stommel boundary layer.

At $r = 1$, and outside the boundary layer near $\theta = 0$, the above solution gives

$$p_I = \frac{2\dot{\zeta}}{F}(\theta-\theta_0). \tag{4.9}$$

A bottom, frictional layer must exist also near $r = 1$ to bring p_I to zero. With

$$\eta = \epsilon^{\frac{1}{2}}(1-r), \quad -\frac{\partial}{\partial r} = e^{-\frac{1}{2}}\frac{\partial}{\partial\eta}, \tag{4.10}$$

the equation becomes

$$\frac{\partial^2 p_I}{\partial \eta^2} + \frac{\partial p_I}{\partial \theta} = 2\dot{\zeta}/F. \tag{4.11}$$

The inhomogeneous solution is given by (4.9). A solution for the homogeneous part of the equation is required to bring p_I to zero at $r = 1$. This is done by seeking a similarity solution of the type,

$$p_I = -\frac{2\dot{\zeta}}{F}(\theta - \theta_0)\, G(\gamma), \quad \gamma = \eta k(\theta), \tag{4.12}$$

for the equation

$$\frac{\partial^2 p_I}{\partial \eta^2} + \frac{\partial p_I}{\partial \theta} = 0, \tag{4.13}$$

where $G(\gamma) = 1$, at $\gamma = 0$ (i.e. $\eta = 0$ or $r = 1$),

$G(\gamma) \to 0$, as $\gamma \to \infty$ (i.e. $\eta \to \infty$),

with $$k(\theta) = [2(\theta_0 - \theta)]^{-\frac{1}{2}}, \quad \gamma = (1-r)\,[2\epsilon(\theta_0 - \theta)]^{-\frac{1}{2}} \tag{4.14}$$

and $$G(\gamma) = \exp(-\gamma^2/4)\, F(\gamma). \tag{4.15}$$

The equation (4.13) yields

$$F''(\gamma) - (\tfrac{5}{2} + \tfrac{1}{4}\gamma^2)\, F(\gamma) = 0, \tag{4.16}$$

whose solution can be written in terms of Weber's parabolic cylinder functions, which have been studied quite thoroughly by Miller. The solution of (4.16), together with the boundary conditions given above may be written in standard form as

$$F(\gamma) = \frac{2^{\frac{3}{2}}}{\sqrt{\pi}}\, U(\tfrac{5}{2}, \gamma), \tag{4.17}$$

where $U(\frac{5}{2}, \gamma)$ is one of the standard Weber's functions which converges to zero as $\gamma \to 0$. It is related to the notation of Whittaker by

$$U(\tfrac{5}{2}, \gamma) = D_{-2}(\gamma).$$

The mathematical form and numerical values of $U(\frac{5}{2}, \gamma)$ are summarized by Miller in Abramowitz & Stegun (1965), and will not be reproduced here.

The total solution for the interior can be written as

$$p_I = \frac{2\dot{\zeta}}{F}\left[(\theta - \theta_0) + \theta_0 \exp(-r^2\theta/\epsilon) - (\theta - \theta_0)\exp(-\gamma^2/4)\,\frac{2^{\frac{3}{2}}}{\sqrt{\pi}}\, U(\tfrac{5}{2}, \gamma)\right]. \tag{4.18}$$

The pressure field represented by (4.18) and calculated for $F = 3{\cdot}19 \times 10^{-2}$, $E = 2 \times 10^{-5}$ is shown in figure 3. The pressure field given by (4.8) corresponds to the stream function in Stommel's oceanic model.

The foregoing solution is the basic one for the pie-shaped basin. However, the solution does not satisfy the non-slip condition along the side walls. A Stewartson layer of thickness $E^{\frac{1}{4}}$ must be added to bring the tangential velocity to zero along the sides, $\theta = 0$ and $\theta = \theta_0$. The $E^{\frac{1}{4}}$ layer derived earlier must be modified in order to include the effects of the strong radial flow near the side walls and of the paraboloidal free surface.

Denote the variables in the $E^{\frac{1}{4}}$ layer by a tilde. Then the free surface condition in the $E^{\frac{1}{4}}$ layer takes the form,

$$\text{at} \quad z = h, \quad \tilde{w} = Fr\tilde{u}. \tag{4.19}$$

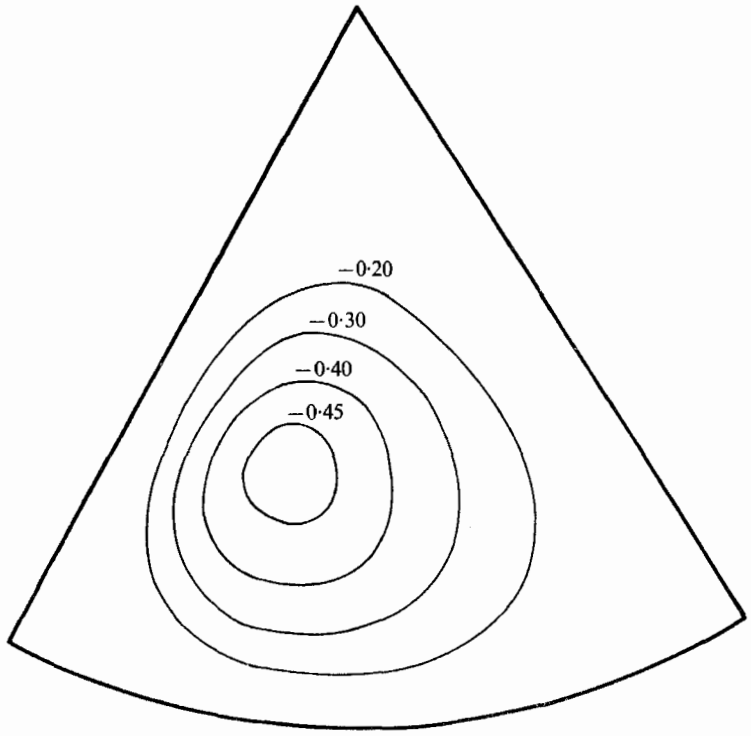

FIGURE 3. The normalized pressure field $p/(\rho\Omega aQ/A)$ of the source-sink flow in a pie-shaped basin ($a = 20$ cm, $\theta = 60°$).

The boundary-layer equations in this case are

$$\left.\begin{aligned} 2\tilde{v} &= \frac{\partial \tilde{p}}{\partial r} - \frac{E}{r^2}\frac{\partial^2 \tilde{u}}{\partial \theta^2}, \\ 2\tilde{u} &= -\frac{1}{r}\frac{\partial \tilde{p}}{\partial \theta}, \\ 0 &= \frac{\partial \tilde{p}}{\partial z}, \\ \frac{1}{r}\frac{\partial}{\partial r}(r\tilde{u}) + \frac{1}{r}\frac{\partial \tilde{v}}{\partial \theta} + \frac{\partial \tilde{w}}{\partial z} &= 0, \end{aligned}\right\} \tag{4.20}$$

where $\tilde{u} = u_0 + E^{\frac{1}{4}}u_1$, $\tilde{v} = E^{\frac{1}{4}}v_0 + E^{\frac{1}{2}}v_1$, $\tilde{p} = E^{\frac{1}{4}}p_0 + E^{\frac{1}{2}}p_1$, $\tilde{w} = E^{\frac{1}{4}}w_1$. The system is closed when subscript 1 variables are taken into account.† The resulting equation

† It should be noted here that this system contains normal velocities of $O(E^{\frac{1}{4}})$, whereas the axisymmetric system discussed earlier has normal velocities of $O(E^{\frac{1}{2}})$. This is a basic difference between the two systems.

for the lowest-order pressure is obtained from (4.20), together with (4.19) and the Ekman-layer contribution (2.11), and takes the form,

$$\frac{1}{r^4}\frac{\partial^4 p_0}{\partial\theta^4} - \frac{1}{hr^2E^{\frac{1}{2}}}\frac{\partial^2 p_0}{\partial\theta^2} - \frac{2F}{Eh}\frac{\partial p_0}{\partial\theta} = 0. \tag{4.21}$$

If the $E^{\frac{1}{4}}$ layer is a sub-boundary layer within the Stommel boundary layer, (4.21) can be solved in two parts, with the last two terms balancing within the Stommel boundary layer, and the first two terms forming the balance in the inner, $E^{\frac{1}{4}}$ layer. However, when $F \sim E^{\frac{1}{4}}$, as in our experimental situation, the Stommel boundary layer and the 'sub-boundary' layer have the same thickness, and it is necessary to treat the two together, i.e. to solve (4.21) with (4.4) as the interior solution.

In this case, (4.21) has two modes near $\theta = 0$, which decay with increasing θ, and one mode near $\theta = \theta_0$, which decays with decreasing θ. The solution near $\theta = 0$ has oscillatory decaying modes when the discriminant,

$$D = -\left(\frac{1}{3hE^{\frac{1}{2}}}\right)^3 + \left(\frac{Fr}{2Eh}\right)^2,$$

is positive and monotonically decaying modes when D is negative. In either case, the solution, correct to $O(E^{\frac{1}{2}})$ and satisfying the boundary conditions

$$\tilde{u}(r,\theta) + u_I(r,\theta) = 0 \quad \text{and} \quad \tilde{v}(r,\theta) + v_I(r,\theta) = 0$$

at $\theta = 0$ and θ_0, can be obtained. (The quantities u_I and v_I in these boundary conditions are obtained from (4.4).) The oscillatory decaying modes correspond to Munk's (1950) ocean circulation model. For the experimental situation described in § 5.1, the solution near $\theta = 0$ has exponentially decaying modes in the region where we compare theory and experiment. The solution for the interior region and the $E^{\frac{1}{4}}$ layers near $\theta = 0$ and $\theta = \theta_0$ is

$$p = \frac{2\dot{\zeta}}{F}\left(\theta - \theta_0 - \frac{1}{r\alpha_3}\right) + \sum_{i=1}^{2} c_i(r)\exp\left(-\alpha_i r\theta\right) + c_3(r)\exp\left[-\alpha_3 r(\theta-\theta_0)\right], \tag{4.22}$$

where

$$\left.\begin{aligned} \alpha_n &= -\frac{2}{\sqrt{(3hE^{\frac{1}{2}})}}\cos\left(\frac{\theta}{3} + 120^0 n\right), \quad n = 1, 2, 3, \\ \cos 3\theta &= \sqrt{27}\,\frac{Frh}{(Eh^2)^{\frac{1}{4}}}, \end{aligned}\right\} \tag{4.23}$$

and

$$\left.\begin{aligned} c_1 &= \frac{2\dot{\zeta}}{F}\frac{1}{\alpha_1-\alpha_2}\left[\frac{1}{r} - \alpha_2\left(\theta_0 + \frac{1}{r\alpha_3}\right)\right], \\ c_2 &= \frac{2\dot{\zeta}}{F}\frac{1}{\alpha_1-\alpha_2}\left[\frac{1}{r} - \alpha_1\left(\theta_0 + \frac{1}{r\alpha_3}\right)\right], \\ c_3 &= \frac{2}{r\alpha_3}\frac{\dot{\zeta}}{F}. \end{aligned}\right\} \tag{4.24}$$

A correction near $r = 1$, similar to the one in § 3 for the symmetric flow, can be added to satisfy the non-slip condition. Since the form of this correction is already known, we shall not present the solution here. Instead, we now go on to include variations in the shapes of the boundaries, in order to determine the effects on the flow patterns.

4.2. *Effect of a curved eastern boundary*

The source-sink flow in a pie-shaped basin with a curved eastern boundary, in which bottom friction dominates, is to be examined here, in order to determine the effect on the interior flow. If the eastern boundary is expressed as

$$\theta_E = \theta_0 g(r), \tag{4.25}$$

the solution corresponding to (4.18) can be written as

$$p_I = \frac{2\dot{\zeta}}{F}\left[\theta - \theta_0 g(r) + \theta_0 g(r)\exp\left(-r^2\theta/\epsilon\right) - (\theta - \theta_0 g(1))\exp\left(-\gamma^2/4\right)\frac{2^{\frac{3}{2}}}{\sqrt{\pi}}U(\tfrac{5}{2},\gamma)\right] \tag{4.26}$$

for the flow outside the western and southern $E^{\frac{1}{4}}$ layers. The interior velocity reads:

$$u_I = -\frac{\dot{\zeta}}{rF}, \quad v_I = \frac{\dot{\zeta}}{F}\theta_0\frac{dg(r)}{dr}. \tag{4.27}$$

Hence, the curved eastern boundary will induce a zonal flow. The direction of the interior flow away from the Stommel boundary layer is

$$\phi = \tan^{-1}\frac{v_I}{u_I} = \tan^{-1}\left(\frac{\theta_0 r\, dg}{dr}\right). \tag{4.28}$$

The effect of the curved eastern boundary on the intense flow in the western Stommel layer can be determined from (4.26). The velocity components are

$$\left.\begin{aligned}\bar{u}_I &= \frac{\dot{\zeta}}{F}\left[\frac{r\theta}{\epsilon}g(r)\exp\left(-r^2\theta/\epsilon\right) - \frac{1}{r}\right],\\ \bar{v}_I &= -\frac{\dot{\zeta}}{F}\left[\left(\theta_0 g(r)\frac{2r\theta}{\epsilon} + \theta_0\frac{dg}{dr}\right)\exp\left(-r^2\theta/\epsilon\right) - \theta_0\frac{dg}{dr}\right].\end{aligned}\right\} \tag{4.29}$$

As indicated by (4.29), the radial and zonal velocities in the intense western boundary flow depend on the shape of the eastern boundary ($\theta_0 g(r)$). The influence of the function $\theta_0 dg/dr$ is present only in the zonal velocity. For the interior flow away from the western boundary, the zonal flow induced by the term $\theta_0 dg/dr$ is of the same order as the radial velocity. Thus, the direction of the flow is influenced significantly by the curved eastern boundary as shown by (4.28). For the intense western flow, the radial velocity is $O(1/\epsilon)$ ($\epsilon \sim 10^{-2}$ in the oceanic case) larger than the zonal velocity. Therefore, the effect of the curved eastern boundary on the direction of the western intense current through the influence of $\theta_0 dg/dr$ on the zonal velocity is of relatively minor importance.

4.3. *Effect of a sloping bottom to the source-sink flow*

Consider a pie-shaped container tilted as shown in figure 4. When the base of the container is tilted, the interior flow will be modified by the boundary condition at the bottom. The base of the tank is bounded laterally by $r = 1$, $\theta = 0$ and $\theta = \theta_0$. The tilting angle of the slanted basin is α, and the co-ordinate of the base is $h' = r\sin\theta\sin\alpha$. The condition at the bottom for the interior vertical flow is obtained under the assumption that the tilting angle α is so small that the horizontal velocities of the interior can be considered parallel to the slanted bottom.

These are used in calculating the flux of the Ekman layer. With the approximation $\cos\alpha \simeq 1$, $\sin\alpha \simeq \alpha$ the Ekman layer flux at $z = h'$ is

$$w_I(r,\theta,h') = \frac{E^{\frac{1}{2}}}{2}\left[\frac{1}{r}\frac{\partial}{\partial r}(rv_I) - \frac{1}{r}\frac{\partial u_I}{\partial\theta}\right] - (u_I\sin\theta + v_I\cos\theta)\,\alpha. \tag{4.30}$$

The equation for the interior flow depends on the Froude number, whose magnitude is restricted as in § 4.1. Equating the vertical velocity from the Ekman layer to that given by (4.30) yields

$$\epsilon\left[\frac{1}{r}\frac{\partial}{\partial r}\left(r\frac{\partial p_I}{\partial r}\right) + \frac{1}{r^2}\frac{\partial^2 p_I}{\partial\theta^2}\right] + \left(1 + \frac{\alpha}{rF}\sin\theta\right)\frac{\partial p_I}{\partial\theta} - \frac{\alpha}{F}\cos\theta\frac{\partial p_I}{\partial r} = 2\dot{\zeta}/F. \tag{4.31}$$

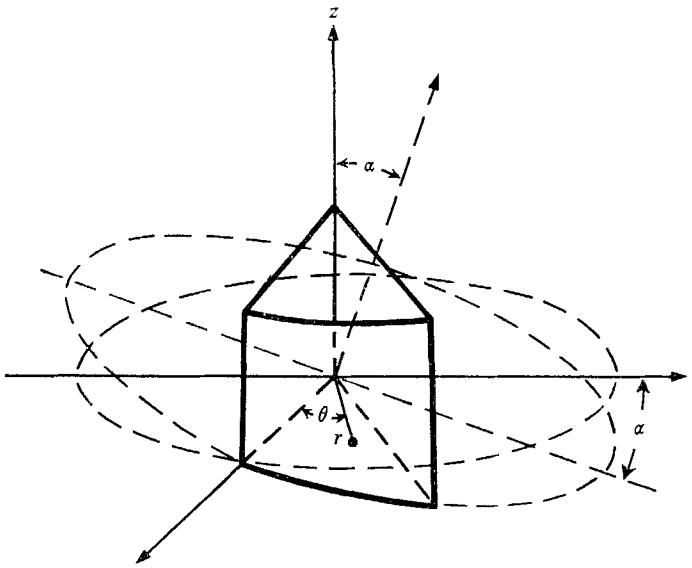

FIGURE 4. A perspective view of the pie-shaped container with a sloping bottom.

The solution satisfying the boundary condition $p_I = 0$ at the sides is obtained by the singular perturbation method of § 4.1. The result reads:

$$\begin{aligned} p_I = \frac{2\dot{\zeta}}{F}\Bigg\{&(\theta-\theta_0) + \sin^{-1}\frac{(\alpha\cos\theta)/F}{(\alpha^2/F^2 + r^2 + 2\alpha r\sin\theta/F)^{\frac{1}{2}}} - \sin^{-1}\frac{(\alpha\cos\theta_0)/F}{(\alpha^2/F^2 + r^2 + 2\alpha r\sin\theta/F)^{\frac{1}{2}}} \\ &+ \left[\theta_0 - \sin^{-1}\frac{\alpha/F}{(\alpha^2/F^2 + r^2)^{\frac{1}{2}}} + \sin^{-1}\frac{(\alpha\cos\theta_0)/F}{(\alpha^2/F^2 + r^2)^{\frac{1}{2}}}\right]\frac{\operatorname{erfc}\left[\left(\frac{\epsilon\alpha r}{2F}\right)^{\frac{1}{2}}\left(\frac{F}{\epsilon\alpha r} + \frac{\theta}{\epsilon}\right)\right]}{\operatorname{erfc}\left[\left(\frac{\epsilon\alpha r}{2F}\right)^{\frac{1}{2}}\left(\frac{F}{\epsilon\alpha r}\right)\right]} \\ &+ \left[\theta_0 - \theta - \sin^{-1}\frac{(\alpha\cos\theta)/F}{(\alpha^2/F^2 + r^2 + 2\alpha r\cos\theta/F)^{\frac{1}{2}}} + \sin^{-1}\frac{(\alpha\cos\theta_0)/F}{(\alpha^2/F^2 + r^2 + 2\alpha r\cos\theta/F)^{\frac{1}{2}}}\right] \\ &\times \exp\left[-(\alpha\cos\theta)\,(1-r)/\epsilon F\right]\Bigg\}. \end{aligned} \tag{4.32}$$

This solution has a form which is considerably more complicated than is the corresponding solution given by the first two parts of (4.18). However, the complication arises only because of the depth variation associated with *both*

the paraboloidal free surface *and* the sloping bottom. The interior solution consists of the terms which involve neither the erfc nor the exponential terms. It is simply a flow from the deepest (south-eastern) corner of the basin to shallower regions. The boundary-layer solution required to bring the normal velocity to zero at $\theta = 0$ and θ_0 is given by the erfc terms. In the limit $\alpha \to 0$, it reduces to the simple exponential term in (4.18). The remaining term describes the boundary layer near $r = 1$ which has thickness of $O(\epsilon)$ as opposed to the thickness of $O(\epsilon^{\frac{1}{2}})$ for the

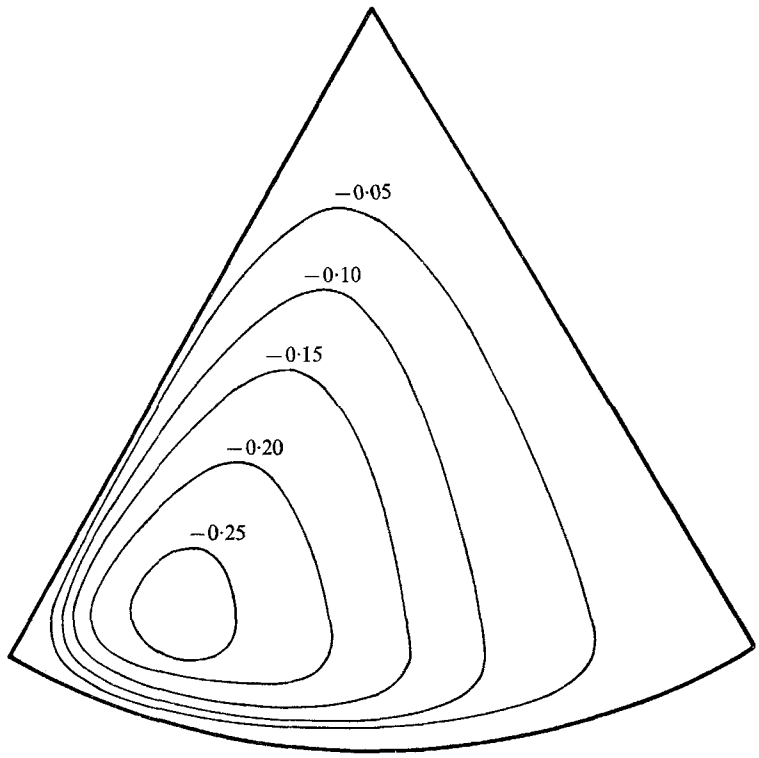

FIGURE 5. The normalized pressure field $p/(\rho\Omega aQ/A)$ of the source-sink flow in the pie-shaped basin with a sloping bottom ($a = 20$ cm, $\theta_0 = 60°$, $\alpha = 5{\cdot}77 \times 10^{-2}$ radian).

corresponding boundary layer in (4.18). The reason for this difference in thickness is that interior flow parallel to the rim is generated by the sloping bottom, and this parallel flow is used in the matching of interior and boundary-layer flow. There is no corresponding parallel flow in the flat-bottom case, so the two solutions are basically different near $r = 1$.

The pressure field represented by this equation is calculated for $\alpha = 5{\cdot}77 \times 10^{-2}$, $E^{\frac{1}{2}} = 2 \times 10^{-5}$, $F = 3{\cdot}19 \times 10^{-2}$, and is shown in figure 5. The corresponding intense velocities in the Stommel boundary layers will be compared with experiments. The solution of p_I given by (4.32) satisfies only the condition that the normal velocity vanishes at the side wall. A viscous boundary layer is required to adjust the non-slip condition. The general nature of this viscous boundary layer has been discussed in previous chapters, and will not be given here. Hence, near the wall the solution will lack agreement with the experimental data.

5. Experimental results

5.1. *Methods*

Experiments were carried out to verify the theoretical results. A plexiglas tank of the desired shape was placed on a horizontal turntable with its vertical axis coincident with the rotating axis. The turntable rotated counter-clockwise, and the rotation rate was measured to an accuracy of 0·1 %. A source of water was introduced by a syringe driven by a constant rotating motor. The influx of the source was $4{\cdot}9 \times 10^{-2}\,\mathrm{cm^3\,sec^{-1}}$. The variation of the viscosity of the water was kept under 1 % by controlling the ambient temperature. A camera pointing downward was mounted on the turntable to record the flow patterns of the experiments. Potassium permanganate was used as a dye to indicate the qualitative nature of the flow. The precise measurement of the fluid velocities was made by a pH indicator technique (Baker 1966).

The sources of errors in the experimental results were mainly: (i) the viscous drag of the wire on the flow passing the wire and (ii) the thermal flow induced by the temperature difference between the working fluid and the air in the laboratory.

The error caused by the viscous drag of the wire was negligible in the measurement of the velocity component perpendicular to the wire, but became quite significant in determining the velocity component parallel to the wire. The effect was kept to a minimum by using very fine wire with diameter 2×10^{-3} in. This error may be eliminated by removing the wire after the dye line is generated.

A temperature difference of 0·2 °C or higher between the working fluid and the surroundings could set up a convection flow, which could be observed when the fluid was supposed to be in solid-body rotation. This thermal effect was eliminated by setting up the experimental arrangement several hours before the actual runs, and allowing the system to come to thermal equilibrium with the room temperature. Also, the working fluid was stored in a large bottle in the laboratory, and consequently was in thermal equilibrium at the time of use. Only those experiments in which no significant thermal convection flow was present are reported.

5.2. *Results*

(*a*) *Flow in a cylindrical container.* The experiment analyzed in § 3 was carried out with a cylindrical container of radius 6·35 cm and a rotation rate of $1{\cdot}25\,\mathrm{rad\,sec^{-1}}$. The height of the fluid in the container was originally 6 cm. A point source was introduced just beneath the free surface at $r = 1$ and $\theta = 0$ by a small tube of 0·5 cm diameter. The influx of the source was $4{\cdot}9 \times 10^{-2}\,\mathrm{cm^3\,sec^{-1}}$, which gave an upwelling velocity of the free surface of $3{\cdot}86 \times 10^{-4}\,\mathrm{cm\,sec^{-1}}$. The Ekman number was $1{\cdot}98 \times 10^{-4}$ with the chosen parameters. The Rossby number was $0{\cdot}55 \times 10^{-3}$ and the Froude number was $9{\cdot}8 \times 10^{-3}$.

Potassium permanganate was used in the source as a dye for visualizing the nature of the distribution of the transport. The source was distributed along the $E^{\frac{1}{3}}$ layer, and was smoothed out by the $O(E^{\frac{1}{2}})$ interior horizontal flow. The fluid was supplied to the bottom Ekman layer via the $E^{\frac{1}{4}}$ layer. The picture in figure 6 (*a*) (plate 1) indicates qualitatively this type of behaviour. The dyed fluid from the source distributed vertically as a line source and spread along the wall and in the

bottom Ekman layer. Pictures of the lines made by pH indicator technique in figures 6(*b*) and (*c*) (plate 1) were taken by applying the d.c. voltage pulse at times separated by 60 sec. The theoretical, normalized zonal velocity $V/(\check{\zeta}/E^{\frac{1}{2}})$, indicated by (3.2) with the $E^{\frac{1}{4}}$ layer correction, is compared with the experimental result in figure 7. A good agreement is clearly indicated. The small deviation (less than 5 %) may be due to the error in measurement of the position of the dye line ($\pm$ 0·05 cm). One can see in figure 6(*c*) that the viscous drag of the wire is more pronounced near the centre, where the zonal velocity is very small.

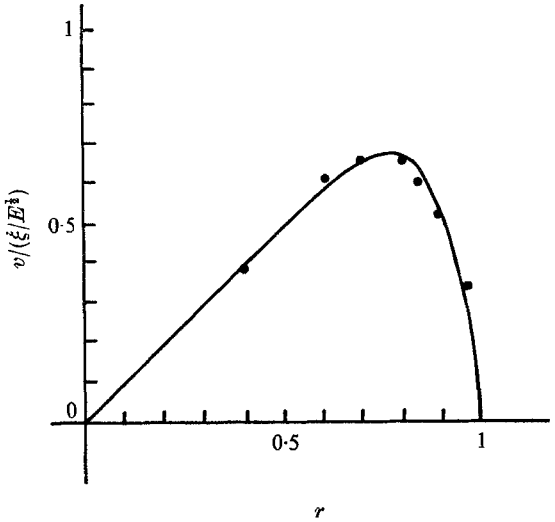

FIGURE 7. The comparison of the theoretical and experimental zonal velocity in the source-sink flow in the rotating cylindrical container shown in figure 6. ——, theoretical value; ●, experimental data.

(*b*) *Flow in pie-shaped basin.* Experiments were set up to verify the results obtained in § 4 for the source-sink flow, in which bottom friction dominates over the side-wall viscous effect. A pie-shaped basin of 60° width, radius 20 cm and height 15 cm was used. The initial height of the fluid was 6 cm. The rotation rate was chosen as 1·25 rad sec^{-1}, which gave $F = 3{\cdot}19 \times 10^{-2}$, $E = 2{\cdot}0 \times 10^{-5}$, $E^{\frac{1}{2}}/2F = 7{\cdot}01 \times 10^{-2}$ and $E^{\frac{1}{4}}/2Fh^{\frac{1}{2}} = 2{\cdot}0$. Hence, the condition that the latter parameter be much larger than unity was not really satisfied. The source at the apex was introduced just beneath the free surface by a tube of diameter 0·5 cm. The strength of the source, $4{\cdot}9 \times 10^{-2}$ cm^3 sec^{-1}, gave an upwelling of the free surface of $2{\cdot}34 \times 10^{-4}$ cm sec^{-1}. The Rossby number of the flow was 3×10^{-4}, which indicated that non-linear effects were not important.

For the experiment in the pie-shaped basin a net of printed platinum wires was introduced, so that the pH indicator method would exhibit a pattern of dashed lines, as shown in figure 8(*a*) (plate 1), when a small voltage was applied. The dashed lines enabled one to evaluate the velocity components in both the r and the θ directions. The flow pattern which results when pulses are separated by 60 sec intervals is shown in figure 8(*c*) (plate 1). The streamline pattern agrees with the corresponding pressure field pattern of figure 3.

Measurements of the velocities were restricted to the flow in the boundary layer, because the interior flow was too slow to be measured accurately. Measured profiles of u and v *vs.* θ near $\theta = 0$ and along $r = 0{\cdot}55$ (11 cm) are compared in figure 9 with the theoretical values calculated from (4.4) and (4.22). The corresponding comparison for u and v *vs.* r near $r = 1$ and along $\theta = 30°$ is shown in figure 10.

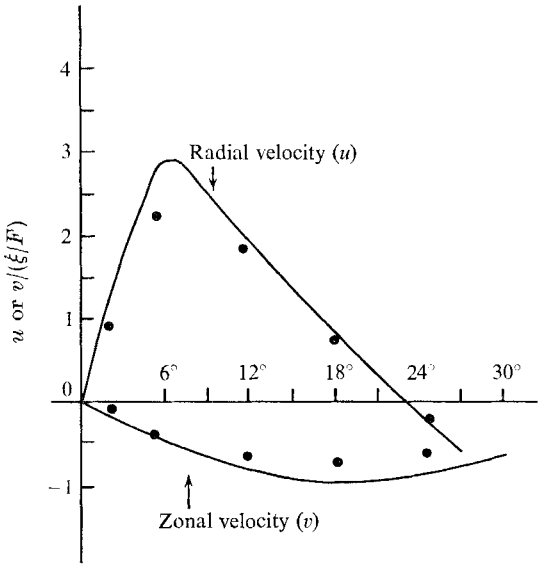

FIGURE 9. The comparison of the theoretical and experimental velocities along $r = 11$ cm ($r = 0{\cdot}55$) near the western boundary ($\theta = 0$) of the source-sink flow in a pie-shaped basin. ——, theoretical value; ●, experimental data.

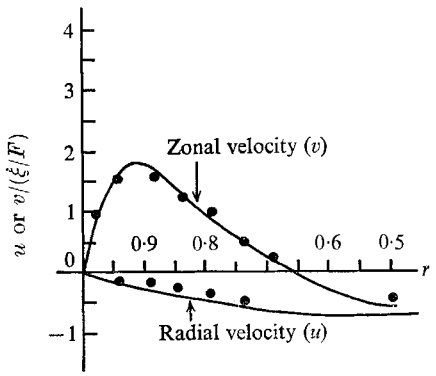

FIGURE 10. The comparison of the theoretical and experimental velocities along $\theta = 30°$ near the southern boundary (outer rim) of the source-sink flow in a pie-shaped basin. ——, theoretical value; ●, experimental data.

For the latter comparison, the theoretical value is calculated from the last term in (4.18), together with the $E^{\frac{1}{4}}$ layer correction, to satisfy the non-slip condition.

The corresponding results for the sloping bottom case are shown in figures 11 (plate 1), 12 and 13. Here, the effects of the $E^{\frac{1}{4}}$ layer have been omitted in the calculations, so that the tangential velocity cannot match the non-slip condition at the boundary.

The general agreement between theory and experiment is quite good. The analytical solutions are not complete, because all of the boundary-layer corrections have not been included. For the flat-bottom case the more important boundary-layer effects have been taken into account and the agreement is better. The uncertainty in the measurement of the displacement of the dye is 0·05 cm, and can also contribute to the lack of agreement.

The experimental verification of the effect of the curved eastern boundary on

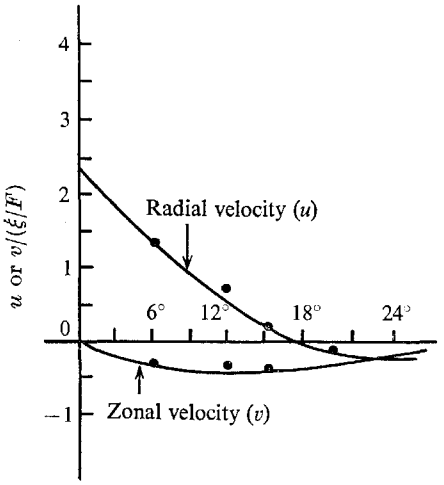

FIGURE 12. The comparison of the theoretical and experimental velocities along $r = 10$ cm ($r = \frac{1}{2}$) near the western boundary ($\theta = 0$) of the source-sink flow in the pie-shaped basin with a sloping bottom. The theoretical solution is for the interior variables only; hence, the lack of agreement for the radial velocity near $\theta = 0$. ——, theoretical value; ●, experimental data.

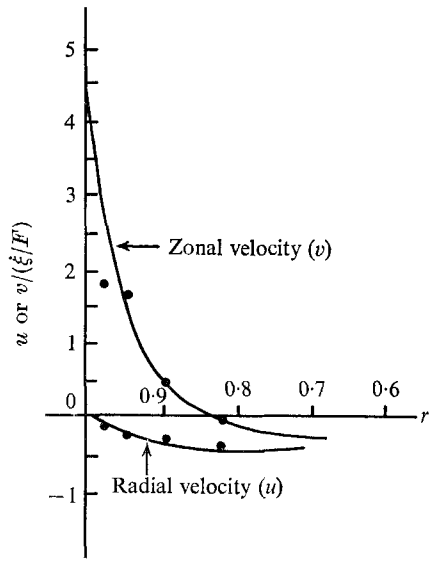

FIGURE 13. The comparison of the theoretical and experimental velocities along $\theta = 30°$ near the southern boundary (outer rim) of the source-sink flow in the pie-shaped basin with a sloping bottom. The theoretical solution is for the interior variables only; hence, the lack of agreement for the zonal velocity near $r = 1$. ——, theoretical value; ●, experimental data.

the interior flow away from the western boundary was carried out in the basin with the flat bottom. Three pie-shaped tanks of radius 20 cm were constructed, with the curved eastern boundary expressed by

(i) $$\theta_E = \tfrac{1}{3}\pi,$$

(ii) $$\theta_E = \tfrac{1}{6}\pi(1 + \tfrac{3}{2}r),$$

(iii) $$\theta_E = \tfrac{1}{2}\pi(1 - \tfrac{1}{2}r).$$

Results using the pH indicator method in each basin are shown in figure 14 (plate 1). A small dot was insulated in the platinum wire near the eastern boundary, so that a discontinued marker line will appear when a small d.c. voltage was applied. The curved lines in figure 14 were photographed 5 min after the pulse was applied. The figures show initial and final position of the dye line. The experiment was performed at the rotation rate of 1·25 rad sec^{-1}, with the strength of the influx source $4{\cdot}9 \times 10^{-2}$ cm^3 sec^{-1}. The insulated point along the wire was located at (14 cm, 45°). Fluid initially at the point (12 cm, 45°) will move in a direction inclined 0°, +25° and −25° to the radial line through the point for the curved eastern boundaries given by (i) (ii) and (iii), respectively. This behaviour was observed, and a qualitative verification is evident in figure 14.

6. Gulf Stream separation experiments

Current charts show the separation of the Gulf Stream and the Kuroshio Current from the coast (see Fuglister 1963; Uda 1964). Although baroclinic effects must be important in the behaviour of these intense currents, particularly with regard to their separation, a partial study of this phenomenon can be made in the laboratory. The interior flow generated by sources and sinks can simulate the effect of a wind-stress at the bottom of the Ekman layer and the variation of free surface height serves the same role as the β-effect in oceanic flows.

Munk (1950), Munk & Carrier (1950), Sarkisyan (1954) and Bryan (1963) have shown that the mean wind patterns over the oceans can generate circulations in which the Gulf Stream and Kuroshio will flow outward from the coast just north of the subtropical, high-pressure, wind gyre. Warren (1962) and Holland (1967) have shown that these intense currents will separate from the coast when they encounter rising bottom topography downstream.

To test these theoretical results two experiments have been performed.

(i) A source of fluid was introduced at the apex of a pie-shaped basin with lateral boundaries at $r = 20$ cm, $\theta = 0$ and $\theta = 60°$ and with a sloping bottom in the southwestern corner (figure 15, plate 2). The rotation rate was 1·25 rad sec^{-1}, and a source with a flux of $4{\cdot}9 \times 10^{-2}$ cm^3 sec^{-1} was introduced just beneath the free surface by a tube of 0·5 cm diameter. Hence, the Ekman number was $E = 2 \times 10^{-5}$ and the Froude number was $F = 3{\cdot}19 \times 10^{-2}$. Pulses of small voltage were applied to the three printed wires, shown in figure 15, at 60 sec intervals, and the flow was determined from the pattern of dashed lines. The thin line paralleling the boundary $\theta = 60°$ shows the junction of the sloping bottom with the flat bottom. The figure gives a clear indication that the intense western

boundary current separates from the $\theta = 0$ boundary and flows parallel to the thin line. This behaviour corresponds to that expected from the studies of Warren and Holland.

(ii) A concentrated sink of fluid at (9 cm, $\frac{1}{6}\pi$) and a concentrated source at (15 cm, $\frac{1}{6}\pi$) were introduced into the pie-shaped basin with the flat bottom. The source and sink are meant to simulate the annual mean atmospheric pressure patterns over either the N. Atlantic or the N. Pacific. The flux through the source and the sink was $4{\cdot}9 \times 10^{-2}\,\mathrm{cm^3\,sec^{-1}}$, and the rotation rate was $2\,\mathrm{rad\,sec^{-1}}$. Figure 16 (plate 2) shows the flow pattern as exhibited by the pH indicator method when the printed wires (shown by the two dashed straight lines) were pulsed at 30 sec intervals. Separation of the intense western boundary currents from the western boundary is evident.

We gratefully ackowledge the support of the National Science Foundation through Grants GA-872, GA-1416 and GA-11410. We are grateful to Dr W. L. Siegmann for a thorough critique of the original manuscript, and for pointing out several shortcomings of the original version of this paper.

REFERENCES

Abramowitz, M. & Stegun, I. A. (eds.) 1965 *The Handbook of Mathematical Functions.* New York: Dover.

Baker, D. J. 1966 A technique for the precise measurement of small fluid velocities. *J. Fluid Mech.* **26**, 573–575.

Barcilon, V. 1967 On the motion due to sources and sinks distributed along the vertical boundary of a rotating fluid. *J. Fluid Mech.* **27**, 551–560.

Beardsley, R. C. 1969 A laboratory model of the wind-driven ocean circulation. *J. Fluid Mech.* **38**, 255–271.

Bryan, K. 1963 A numerical investigation of a non-linear model of a wind-driven ocean. *J. Atmos. Sci.* **20**, 594–606.

Cole, J. D. 1968 *Perturbation Methods in Applied Mathematics.* London: Blaisdell.

Fuglister, F. C. 1963 Gulf Stream '60. *Progress in Oceanography* (Sears, ed.), vol. 1, ch. 5. London: Pergamon.

Greenspan, H. P. 1968 *The Theory of Rotating Fluids.* Cambridge University Press.

Hide, R. 1967 On source-sink flows in a rotating flow. *J. Fluid Mech.* **32**, 737–764.

Holland, W. R. 1967 On the wind-driven circulation in an ocean with bottom topography. *Tellus*, **19**, 582–599.

Munk, W. H. 1950 On the wind-driven ocean circulation. *J. Meteorol.* **7**, 79–93.

Munk, W. H. & Carrier, G. F. 1950 On the wind-driven circulation in ocean basins of various shapes. *Tellus*, **2**, 158–167.

Pedlosky, J. & Greenspan, H. P. 1967 A simple laboratory model for the oceanic circulation. *J. Fluid Mech.* **27**, 291.

Sarkisyan, A. C. 1954 The calculation of stationary wind currents in an ocean. *Izv. Acad. Nauk SSSR, Ser. Geofiz.* **6**, 554–561.

Stewartson, K. 1957 On almost rigid rotations. *J. Fluid Mech.* **3**, 17–26.

Stommel, H. 1948 The western intensification of wind-driven ocean currents. *Trans. Am. Geoph. Union*, **29**, 202–206.

Stommel, H. 1957 A survey of ocean current theory. *Deep-Sea Res.* **4**, 149–184.

Stommel, H., Arons, A. B. & Faller, A. J. 1958 Some examples of stationary planetary flows. *Tellus*, **10**, 179–187.

SVERDRUP, H. U. 1947 Wind-driven currents in a baroclinic, with application to the equatorial currents of the eastern Pacific. *Proc. Natn. Acad. Sci. U.S.A.* **33**, 318–326.

UDA, M. 1964 On the nature of the Juroshio, its origin and meanders. *Studies on Oceano graphy*, 89–107.

WARREN, B. A. 1963 Topographic influences on the Gulf Stream. *Tellus*, **15**, 167–183.

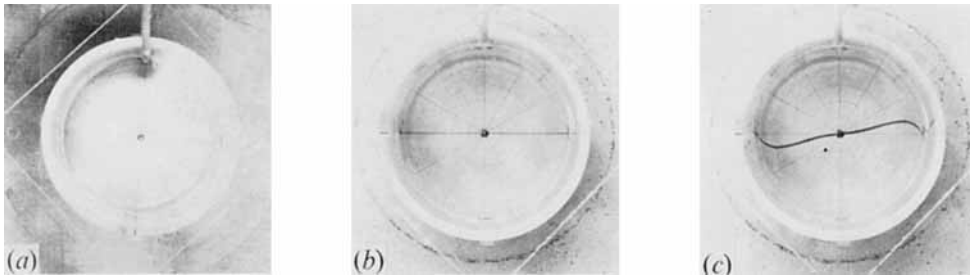

FIGURE 6. The experiments on the source-sink flow in a rotating cylindrical container.

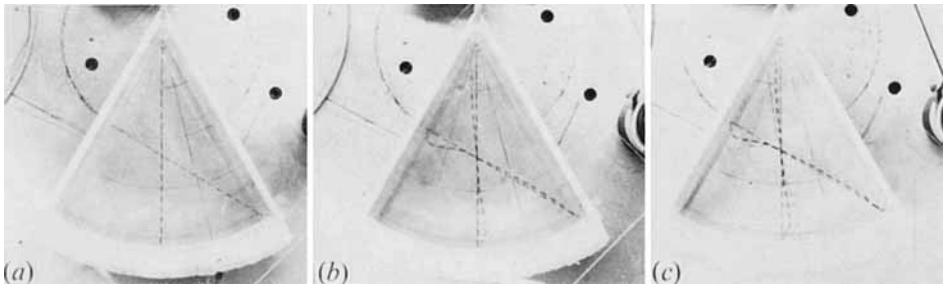

FIGURE 8. The experiments on the source-sink flow in a pie-shaped basin. The pattern of trajectories can be determined by the movement of the broken lines. Photographs of the patterns were made when the wire was pulsed (at 60 sec intervals).

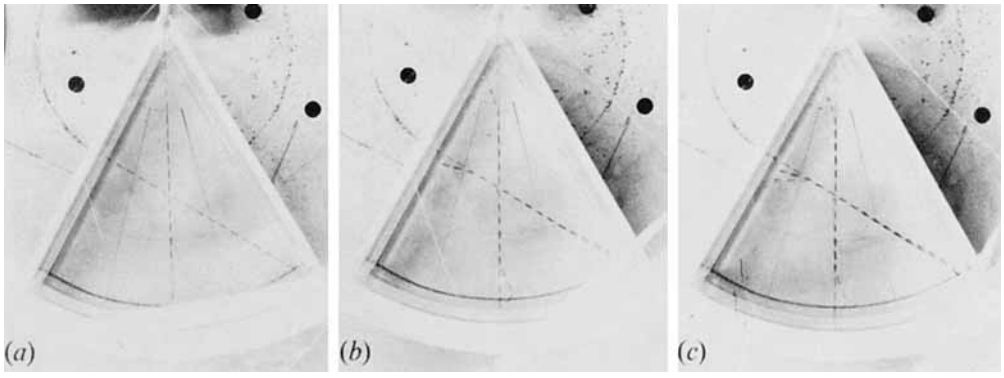

FIGURE 11. The experiments on the source-sink flow in a pie-shaped basin with a sloping bottom.

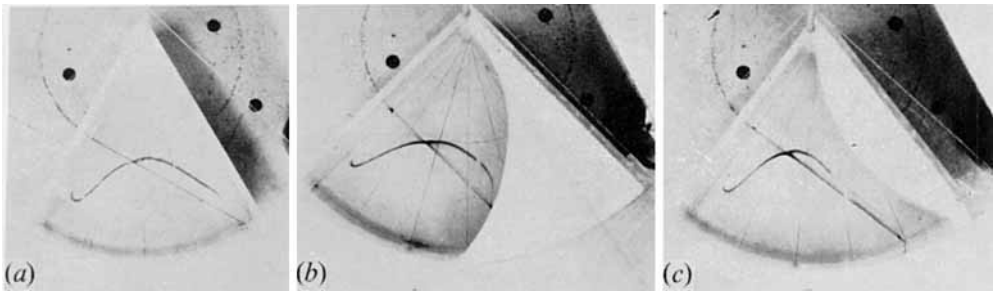

FIGURE 14. The interior flow patterns due to different shapes of the eastern boundary. The curved indicator represents the position of a line of fluid 5 min after it was generated along the straight line joining the end-points. The open dash indicates the zonal displacement of the fluid.

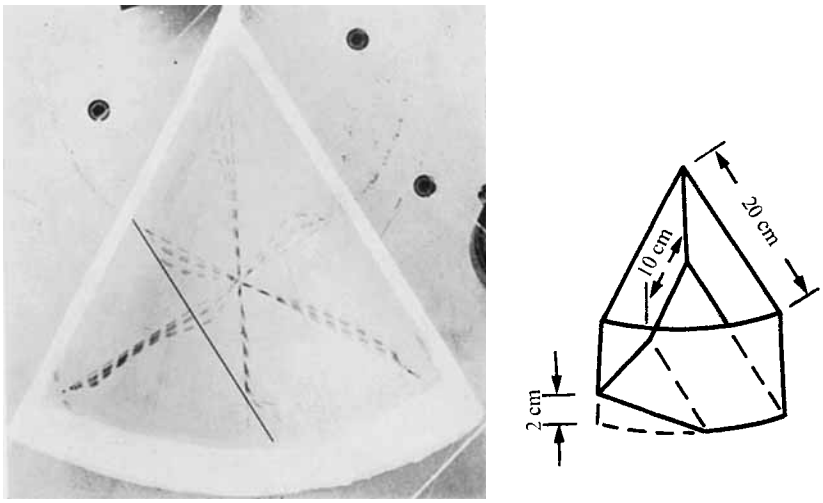

FIGURE 15. The flow pattern due to the source-sink flow in the pie-shaped basin with a partially sloping bottom. The intense current leaves the western boundary ($\theta = 0$) at $r = 0{\cdot}5$ and flows parallel to the line joining the sloping region to the bottom.

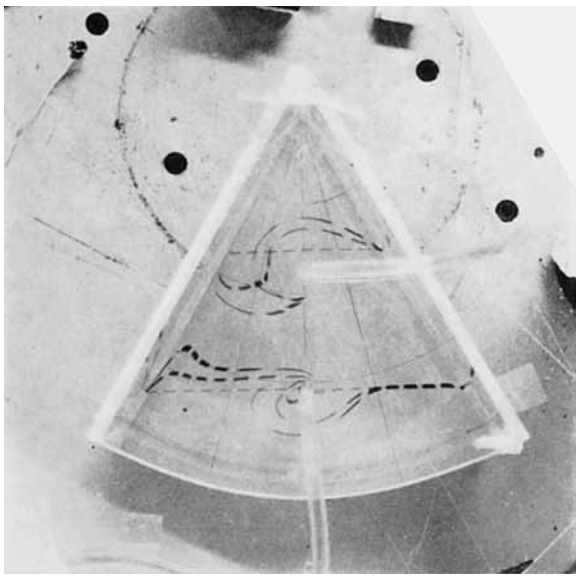

FIGURE 16. The flow pattern due to the concentrated source and sink in a pie-shaped basin. The converging western boundary currents leave the boundary and move into the interior in a region between the source and sink.